Article

Bicubic splines for fast-contracting control nets

Kęstutis Karčiauskas[1], Kyle Lo[3], Erkan Gunpinar [2], and Jörg Peters[3,*] 0000-0002-2499-1529

[1] Institute of Mathematics, Vilnius University, Lithuania; kestutis.karciauskas@mif.vu.lt
[2] Department of Mechanical Engineering, Istanbul Technical University;, Türkiye; gunpinar@itu.edu.tr
[3] Department of Computer and Information Sciences and Engineering, University of Florida, USA; jorg.peters@gmail.com
* Correspondence: jorg.peters@gmail.com

Abstract: Merging parallel quad strips facilitates narrowing surface passages, and allows a design to transition to simpler shape. While a number of spline surface constructions exist for the isotropic case where n pieces join, few existing spline constructions deliver good shape for control-nets that merge parameter lines; and, until recently, none provided good shape for fast-contracting polyhedral control-nets. This work improves the state-of-the-art of piecewise polynomial spline surfaces accommodating fast-contracting control nets. The new fast-contracting (FC) surface algorithm yields the industry-preferred uniform degree bi-3 (bi-cubic), the surfaces are by default differentiable, have improved shape, measured empirically as highlight line distribution, and require fewer pieces than the state-of-the-art.

Keywords: polyhedral-net spline; control-net contraction; geometric continuity
MSC: 68U07 Computer science aspects of computer-aided design, 65D17 Computer-aided design (modeling of curves and surfaces)

1. Introduction

To accommodate narrower surface passages or account for less shape fluctuation, a designer can merge parallel parameter lines as illustrated in Fig. 1 a,b, see the gray regions. Aggressive merging in in quad-meshing algorithms such as [1,2] packs the gray contraction regions too close to each other as in Fig. 1 c,d: existing algorithms require these faces to be separated by a frame of quadrilaterals. Mitigation strategies range from ad hoc designer intervention, to an improved Doo-Sabin refinement step [3,4], to special re-meshing rules for T_0- and T_1-locations, [5], see Fig. 1 e. The drawback of these mitigations is both an increase in the number of patches and a decrease in the surface quality. Surface quality suffers since, to obtain the required combinatorial structure, the natural cross field (flow) of the geometry is disturbed.

The recent publication [6] therefore presented two new Fast Contracting (FC) spline constructions: FC^4 and FC^3. FC^4 generates surfaces of bi-degree (2, 4) or (2, 3), FC^3 of bi-degree 3. Both assume that the regular quad-grid of the control net define bi-2 C^1 splines, and both use as control net the un-isotropic $\triangle^2$ configuration of Fig. 1 f, that retains the two preferred directions of the tensor-product splines. The split of the gray core is ignored and no re-meshing or refinement is required to guarantee geometric G^1 continuity of the resulting surfaces.

Unlike FC^3, the new bi-3 construction FC^3_8 manages the transition from two (top) to four (bottom) bi-3 pieces via two internal T-junctions, and requires only the two T-junctions of the center line, see Fig. 2 (e) vs (f). Remarkably,

- FC^3_8 is a 8-piece bi-3 (bi-cubic) construction.
- FC^3_8 yields improved shape compared to FC^3, measured empirically as more uniform highlight line distribution, and has fewer polynomial pieces, the minimal number required for good shape.
- The FC^3_8 formulas for generating bi-3 patches are linear in the input control net, hence can be collected into a matrix.
- Implementation of FC^3_8 can so be reduced to: gathering the control net in a vector of points and multiplying the vector by a matrix.

Citation: Karčiauskas, K.; Lastname, F.; Peters, J. Bicubic splines for fast-contracting control nets. *Axioms* **2024**, *1*, 0. https://doi.org/

Received:
Revised:
Accepted:
Published:

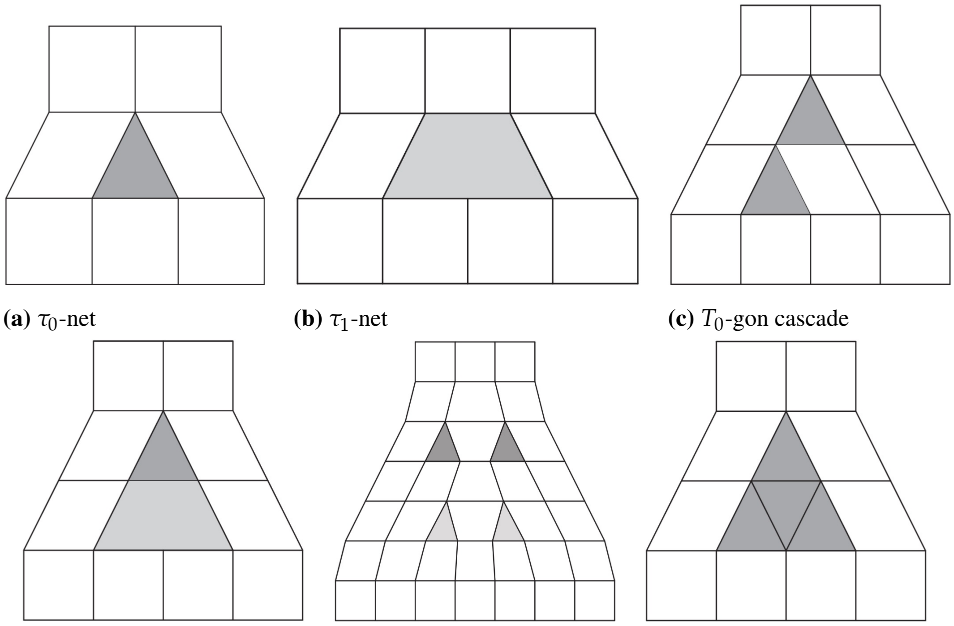

(a) τ_0-net **(b)** τ_1-net **(c)** T_0-gon cascade

(d) T_0-gon above T_1-gon **(e)** refinement [5] **(f)** $\triangle^2$-net [6]

Figure 1. Contracting control-net configurations: one strip contraction in a (a) τ_0-net and (b) τ_1-net from [7,8] and two-strip contraction via (c) cascading triangles, (d) T_0-gon + T_1-gon and (e) refinement according [5]; (f) $\triangle^2$-net with triangulated gray core as a generalization of (c) and (d): removing from the core one inner bottom edge yields (c), removing both yields (d).

The patch count can be further reduced to 7 by merging the two middle patches of FC^3_8, but, as is demonstrated, this diminishes the resulting surface quality significantly.

We note that tensor product splines (NURBS) are the preferred representation in many modeling packages and degree bi-3 (bi-cubic) is the preferred degree. Catmull-Clark subdivision surfaces [9], popular in computer graphics, are also of degree bi-3 but consist of an infinite sequence of nested rings generated by recursion. More importantly however, Catmull-Clark and bi-2 Doo-Sabin [3] subdivision rules, are for treating control net configurations with n directions equally, i.e. *isoptroically*, whereas FC splines retain the two preferred direction of the bivariate tensor-product splines. That is, FC splines are more general than tensor-products in that they allow merging of quad strips.

After a brief literature review, Section 2 introduces the technical nomenclature and reviews the existing constructions FC^3 and FC^4. Section 3 introduces and derives the new $\triangle^2$-net construction with explicit tables for implementation. Section 4 provides example-driven critical assessment and discussion of variants as well a comparison to FC^3. For rotationally-symmetric scenarios that permit regular layout or less contraction FC^3_8 is shown to be at least as well-shaped as regular bi-2 splines and the surfaces of [8].

1.1. Related work

FC constructions assemble a finite number of polynomial pieces to join smoothly after a change of variables. Such G^k constructions complement constructions for isotropic configurations such as rational multi-sided surfaces [10–12], and singularly parameterized surfaces. The sub-genres of singular constructions are subdivision surfaces [3,9,13,13–15], edge collapse, polar surfaces [16–18], and vertex singular surfaces [19–22] or rational singular constructions [23,24].

The shape of G^2 constructions of degree bi-7 [25] or degree bi-6 [26], and lower-degree tangent-continuous splines [27–33] is empirically measured via highlight line distribution, [34]. FC surfaces fill irregularities in a C^1 bi-quadratic (bi-2) tensor-product surface, which is attractive since bi-2 splines have minimal bi-degree for smoothing quadrilateral meshes. Subdivision generalizations of bi-2 splines consist of an infinite sequence of nested (contracting) bi-2 polynomial surface rings. [3] has visible artifacts already in the first ring, Augmented Subdivision [4] improves shape by

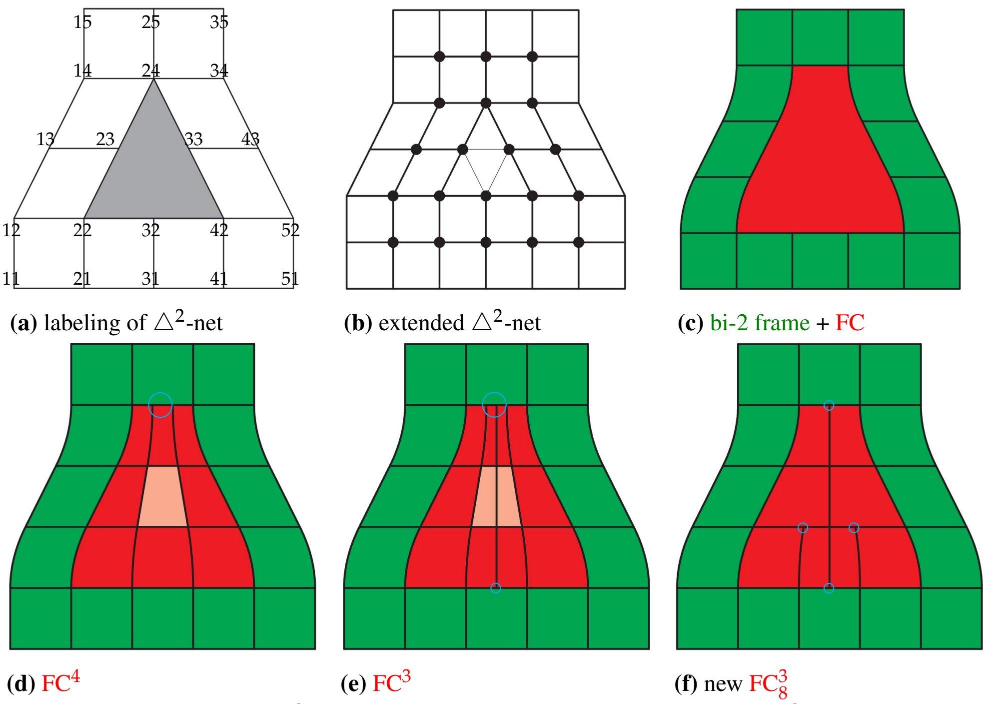

Figure 2. Rapid contraction: (a) $\triangle^2$-net with 20 labels of its nodes $\mathbf{d}_{ij}$. (b) Extended $\triangle^2$-net allows to produce via B-to-BB conversion one bi-2 frame as shown in (c,d,e,f). Bottom row: layouts of FC^4 and FC^3 from [6] and FC$^3_8$.

following a carefully chosen central guide point and Polyhedral-net Splines [35] combine algorithms from [18,36,37] to generalize tensor-product bi-quadratic (bi-2) splines, filling in a *finitely many* polynomial pieces of degree at most bi-3. T-splines [38] address the merging parallel quad strips but typically serve only to refine an existing quad partition: due to their global parameterization requirement, they may not be well-defined for a given T-configuration, see [39, Fig 2], [40, Fig 6]. Alternatively, T-junctions in the control net can be associated with smooth surfaces of bi-degree $(2,4)$ ([7]) or bi-3 ([8]) that result in smooth surfaces of good quality. FC$^3_8$ is partly motivated by the output of quad-dominant meshing algorithms such as [1,2], that introduce (fast) mesh contractions. We note, that the present paper does not touch re-meshing [41–43], but focuses on frequently occurring contracting configurations.

2. Control nets, macro-patches, FC^3 and FC^4

FC$^3_8$ is an improvement of FC^3. We therefore use the notation of [6]. As do tensor-product spline control nets the $\triangle^2$ nets have two distinguished directions that we refer to as 'vertical' and 'horizontal' due to their layout in Fig. 2 . The number of mesh lines is reduced or expanded only in the vertical direction.

2.1. Control nets

Fig. 2 a displays the labels of $\triangle^2$-net used for derivation and presentation of pre-calculated data. The bottom row of Fig. 2 compares the patchworks of three FC surfaces. FC^4, see Fig. 2 d, consists of pieces of bi-degree $(2,4)$ (i.e. 2 in the horizontal direction) except for a middle row of bi-degree $(2,3)$. The central, light-red patch serves as a model for the bi-3 constructions. For FC^3, see Fig. 2 e, this central patch is degree-raised to bi-3 and split into two to keep a tensor-product structure of red macro-patch. The layout of the bi-3 pieces of FC$^3_8$ is shown in Fig. 2 f. The circles in Fig. 2 (d,e,f) mark the locations of T-junctions: small ◦ points to a single T-junction, ◯ to multiple T-junctions. The two T-junctions in (d) merge three strips into one. The additional T-junctions in (e) follow from the fact, proven in [6], that any C^1 bi-3 construction requires an even number of pieces, both at the bottom and the top.

2.2. Polynomial pieces

FC_8^3 consists of tensor-product pieces of polynomial bi-degree (d, d') in Bernstein-Bézier form (*BB-form*, [44]). That is, for Bernstein polynomials $B_k^d(t) := \binom{d}{k}(1-t)^{d-k}t^k$, the bi-degree 3 (bi-3) patch $\mathbf{p}$ is defined as

$$\mathbf{p}(u,v) := \sum_{i=0}^{3}\sum_{j=0}^{3} \mathbf{p}_{ij} B_i^3(u) B_j^3(v), \quad 0 \le u, v \le 1.$$

With the convention that u is the parameter tracing out the horizontal direction.

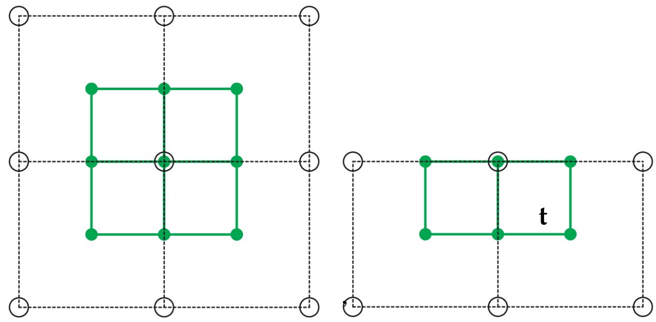

(a) bi-2 **(b)** tensor-border

Figure 3. B-to-BB conversion and tensor-borders $\mathbf{t}$ as Hermite input data. Circles $\circ$ mark B-spline control points, solid disks $\bullet$ mark BB-coefficients of the full patch, respectively tensor-border.

Connecting the *BB-coefficients* $\mathbf{p}_{ij} \in \mathbb{R}^3$ to $\mathbf{p}_{i+1,j}$ and $\mathbf{p}_{i,j+1}$ wherever well-defined yields the *BB-net*, see Fig. 3 . Any 3×3 grid can be interpreted as the control net of a uniform bi-2 spline in uniform knot B-spline form. In Fig. 3 the B-spline control points are marked $\circ$. The *B-to-BB conversion* (e.g. by knot insertion) expresses the spline in bi-2 BB-form illustrated by the green BB-nets in Fig. 3 . Conversion of a partial sub-grid yields a partial BB-net $\mathbf{t}$, called *tensor-border*, that defines position and first derivatives across an edge.

The changing number of mesh lines forces a change of parameterization and hence introduction of *geometric continuity*: Two polynomial pieces $\mathbf{p}, \mathbf{q} : \mathbb{R}^2 \to \mathbb{R}^3$ join G^1 along the common curve with BB-coefficients $\mathbf{p}_{i0} = \mathbf{q}_{i0}$ if there exists a reparameterization $\rho : \mathbb{R}^2 \to \mathbb{R}^2$, see e.g. [45],

$$\mathbf{p}(u,v) := \mathbf{q} \circ \rho(u,v), \qquad \rho(u,v) := (u + b(u)v, a(u)v) \tag{1}$$

$$\partial_v \mathbf{q}(u,0) = a(u)\partial_v \mathbf{p}(u,0) + b(u)\partial_u \mathbf{p}(u,0) \tag{2}$$

for scalar-valued, univariate functions a and b. Besides the shared BB-coefficients of the common boundary, only the layers of BB-coefficients $\mathbf{p}_{i1}$ and $\mathbf{q}_{i1}$ of adjacent patches enter the G^1 continuity constraints. In the derivation, u-, v-directions can be assigned as convenient, but typically u is used to parameterize along the boundary and v in the orthogonal direction of the tensor-border, towards the interior or core.

2.3. Summary of FC^4 and FC^3

The bi-2 tensor-border frame (darkgreen in Fig. 4 a) represents first-order Hermite data. This input for all FC constructions stems from the $\triangle^2$-net by B-to-BB conversion.

Fig. 4 summarizes the construction of FC^4. The khaki-colored bottom layer in (a) is degree-raised to bi-degree $(2, 4)$ and the yellow top layer is uniformly split into 3 pieces and degree-raised. The light-green left and right layers are the result of reparameterizing the left pieces $\mathbf{t}^0$, $\mathbf{t}^1$, $\mathbf{t}^2$, respectively the right pieces $\mathbf{t}^3$, $\mathbf{t}^4$, $\mathbf{t}^5$ of input tensor-border frame. Unconstrained BB-coefficients, are marked $\bullet$, and the BB-coefficients marked $\times$ are defined by C^1 extension of the central (light-red) patch. The remaining BB-coefficients are the averages of their horizontal (black and light-green) neighbor BB-coefficients.

The construction of FC^3 is summarized in Fig. 6 . In (a), leaving $\mathbf{t}_i$, $i = 0, \ldots, 5$, from Fig. 4 a and $\underline{\mathbf{t}}_0$ and $\underline{\mathbf{t}}_3$ unchanged. $\underline{\mathbf{t}}_1$ and $\underline{\mathbf{t}}_2$ represent a uniformly split piece at the middle of the bottom

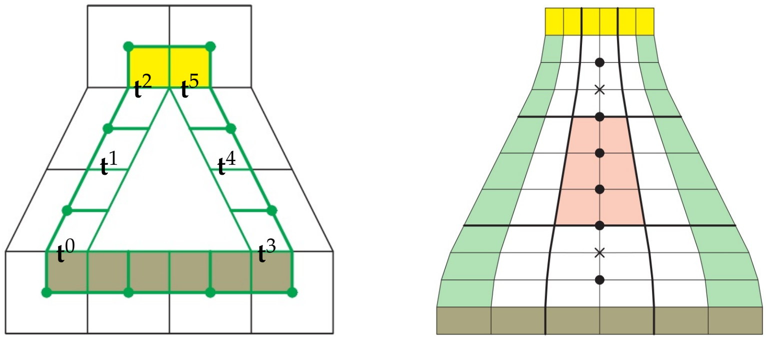

(a) input bi-2 tensor-border frame **(b)** detailed structure of FC^4

Figure 4. FC^4 review: (a) $\triangle^2$-net and input bi-2 tensor-border frame obtained from $\triangle^2$-net by B-to-BB conversion. (b) 3×3 macro-patch structure in BB-form.

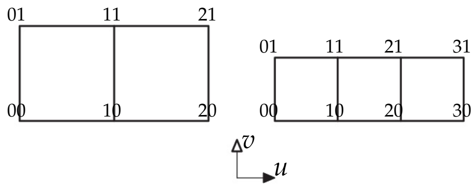

Figure 5. Labeling of: *left* – bi-2 tensor-border; *right* – reparameterized bi-3 tensor-border.

frame of Fig. 4 a. Mimicking the bottom split, $\bar{\mathbf{t}}_i$, $i = 0, \ldots, 3$, top split with ratio $1 : \frac{1}{2} : \frac{1}{2} : 1$. In (b), the reparameterized pieces $\mathbf{t}_i$, $i = 0, \ldots, 5$, $\underline{\mathbf{t}}_i$, $i = 0, \ldots, 3$ and $\bar{\mathbf{t}}_i$, $i = 0, \ldots, 3$ (light-green) are consistent at all four corners and the light-red bi-3 patches 6 and 7 represent the central light-red bi-degree $(2, 3)$ patch from Fig. 4 b, after-degree raising and split. The reparameterizations ρ^s, $s = 0, 1, 2$, $\underline{\rho}^s$, $s = 0, 1, 2, 3$ and $\bar{\rho}^s$, $s = 0, 1$ are also used in FC$^3_8$ construction, see Fig. 5 for the labeling. Formulas (3) and (4) define the bi-3 tensor-border frame (light-green in Fig. 6 b) due to the symmetries $\rho^{3+s} := \rho^s$, $s = 0, 1, 2$.

$$
\begin{aligned}
\rho^s(u, v) :=& (u, a^s(u)), \; a^s(u) := a^s_0(1-u) + a^s_1 u; \; \tilde{\mathbf{t}}^s := \mathbf{t}^s \circ \rho^s; \\
[a^0_0, a^0_1] :=& [1, \frac{7}{9}], \; [a^1_0, a^1_1] := [\frac{7}{9}, \frac{5}{9}], \; [a^2_0, a^2_1] := [\frac{5}{9}, \frac{1}{3}]; \\
\tilde{\mathbf{t}}^s_{01} :=& (1 - \frac{2}{3} a^s_0) \mathbf{t}^s_{00} + \frac{2}{3} a^s_0 \mathbf{t}^s_{01}, \\
\tilde{\mathbf{t}}^s_{11} :=& (\frac{1}{3} - \frac{2}{9} a^s_1) \mathbf{t}^s_{00} + (\frac{2}{3} - \frac{4}{9} a^s_0) \mathbf{t}^s_{10} + \frac{2}{9} a^s_1 \mathbf{t}^s_{01} + \frac{4}{9} a^s_0 \mathbf{t}^s_{11}.
\end{aligned}
\tag{3}
$$

The boundary BB-coefficients $\tilde{\mathbf{t}}^s_{i0}$, $i = 0, \ldots, 3$, are obtained from $\mathbf{t}^s_i$, $i = 0, 1, 2$ by degree-raising. The remaining BB-coefficients $\tilde{\mathbf{t}}^s_{21}$ and $\mathbf{t}_{31}$ are defined by the symmetry $\mathbf{t}^s_{ij} \leftrightarrow \mathbf{t}^s_{2-i,j}$, $i = 0, 1, 2$, $j = 0, 1$; $a^s_i \leftrightarrow a^s_{1-i}$, $i = 0, 1$.

The bottom reparameterizations $\underline{\rho}^s$ and top reparameterizations $\bar{\rho}^s$, $s = 0, 1, 2, 3$, are defined by formulas

$$
\underline{\rho}^s := (u + \underline{\gamma}^s B^2_1(u) v, v), \underline{\gamma}^s := \frac{(-1)^{s+1}}{9}; \; \bar{\rho}^s := (u + \bar{\gamma}^s B^2_1(u) v, v), \bar{\gamma}^s := \frac{(-1)^s}{3}.
$$

Setting $\gamma := \underline{\gamma}^s$, $\mathbf{p} := \underline{\mathbf{t}}^s$, $\mathbf{q} := \tilde{\underline{\mathbf{t}}}^s$ in (4), yields explicit formulas for the BB-coefficients of the reparameterized bi-3 tensor-border $\tilde{\underline{\mathbf{t}}}^s := \underline{\mathbf{t}}^s \circ \underline{\rho}^s$. Setting $\gamma := \bar{\gamma}^s$, $\mathbf{p} := \bar{\mathbf{t}}^s$, $\mathbf{q} := \tilde{\bar{\mathbf{t}}}^s$ in (4) yields $\tilde{\bar{\mathbf{t}}}^s := \bar{\mathbf{t}}^s \circ \bar{\rho}^s$.

$$
\begin{aligned}
\mathbf{q}_{01} :=& \frac{1}{3} \mathbf{p}_{00} + \frac{2}{3} \mathbf{p}_{01}, \; \mathbf{q}_{31} := \frac{1}{3} \mathbf{p}_{20} + \frac{2}{3} \mathbf{p}_{21}, \\
\mathbf{q}_{11} :=& (\frac{1}{9} - \frac{4}{9} \gamma) \mathbf{p}_{00} + (\frac{2}{9} + \frac{4}{9} \gamma) \mathbf{p}_{10} + \frac{2}{9} \mathbf{t}_{01} + \frac{4}{9} \mathbf{p}_{11}, \\
\mathbf{q}_{21} :=& (\frac{2}{9} - \frac{4}{9} \gamma) \mathbf{p}_{10} + (\frac{1}{9} + \frac{4}{9} \gamma) \mathbf{p}_{20} + \frac{4}{9} \mathbf{p}_{11} + \frac{2}{9} \mathbf{p}_{21},
\end{aligned}
\tag{4}
$$

the boundary BB-coefficients $\mathbf{q}_{i0}$, $i = 0, 1, 2, 3$, are obtained from $\mathbf{p}_{i0}$, $i = 0, 1, 2$, by degree-raising.

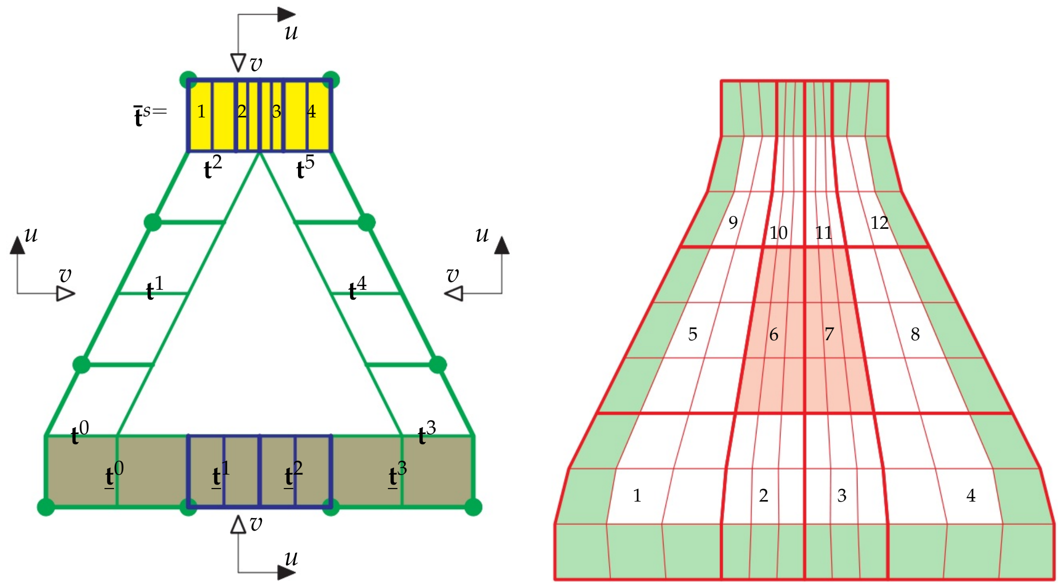

(a) input bi-2 frame after split **(b)** bi-3 BB-net of FC^3

Figure 6. FC^3: (a) The input bi-2 frame is split (see blue top, bottom). The local u-v- coordinate systems of the tensor-borders are shown. (b) Layout of patches and BB-nets of FC^3.

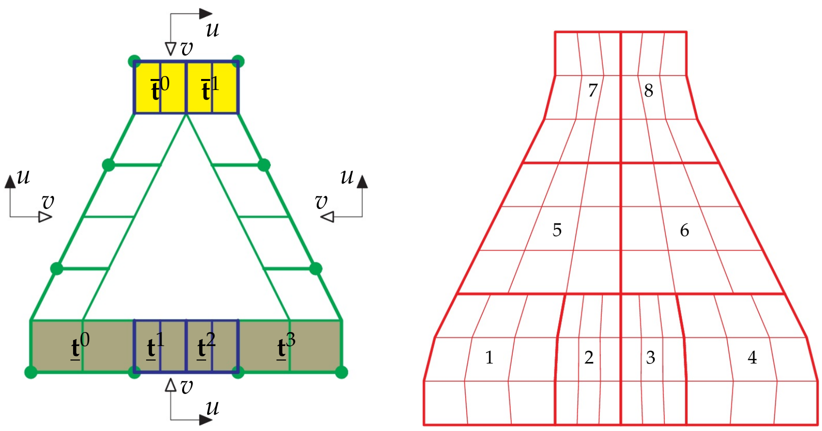

(a) input bi-2 data after split **(b)** bi-3 BB-net and labeling of FC^3_8

Figure 7. FC^3_8: (a) The bi-2 tensor-border frame required for FC^3_8 coincides with the frame in Fig. 6 a except at the top (yellow) that is *uniformly* split into two pieces. (b) BB-net and labeling of the FC^3_8 macro-patch.

3. The FC^3_8 construction

Starting with the bi-2 tensor-border frame, see Fig. 7 a, of FC^3, cf. Fig. 6 a, but, anticipating the layout displayed in Fig. 7 b, *uniformly* splitting the top, we construct the bi-3 tensor-border frame (light-green in (a)) according to Section 2.3, Fig. 6 , and the reparameterized tensor-borders $\tilde{\mathbf{t}}^1$, $\tilde{\mathbf{t}}^2$ (and analogously $\tilde{\mathbf{t}}^4$, $\tilde{\mathbf{t}}^5$) in Fig. 8 a re-scaled as $\bullet := \frac{3}{2}\bullet$- $\frac{1}{2}\bullet$ (Hermite data: $\bullet$ on the boundary remain unchanged). All data of $\mathbf{p}^5$ in Fig. 8 b is displayed in Fig. 8 a,middle-left and again, enlarged, in Fig. 8 c,d: The light-red underlaid piece in Fig. 8 c represents bi-3 patch in Fig. 6 b with label 6. Leaving $\times$ unchanged, we set the BB-coefficients marked $\times := 3\times - 2\times$, to form the layer $\mathbf{p}^5_{2j}$, $j = 0, \ldots, 3$ in Fig. 8 b. The BB-coefficients $\mathbf{p}^6_{1j}$, $j = 0, \ldots, 3$ are constructed analogously. By construction, $\mathbf{p}^5_{3j} = \mathbf{p}^6_{0j}$, $j = 0, \ldots, 3$ and $\mathbf{p}^5_{3j} := \frac{1}{2}\mathbf{p}^5_{2j} + \frac{1}{2}\mathbf{p}^6_{1j}$. On top, the re-scaled tensor-border is reparameterized by $\bar{\rho}_0$, $\bar{\rho}_1$ defined in Section 2.3 yielding $\bar{\mathbf{t}}_0$, $\bar{\mathbf{t}}_1$, see Fig. 7 a. By inspection, the parameterization are consistent at the top two corners in Fig. 8 b. The patches $\mathbf{p}^7$ and $\mathbf{p}^8$ are completed by light-gray extension of patches $\mathbf{p}^5$, $\mathbf{p}^6$, see Fig. 8 b. The patches $\mathbf{p}^s$, $s = 1, \ldots, 4$, are completed by dark-gray extension of patches $\mathbf{p}^5$, $\mathbf{p}^6$ and a subsequent split.

FC^3_8 expresses the BB-coefficients as an affine combinations of the $\triangle^2$-net nodes $\mathbf{d}$. That is, with the formulas of Section 2.3 explicit formulas are available once the BB-coefficients of the central patches are known (light-red in Fig. 6 b). These can be gleaned from [6], but here we present the explicit weights μ of formulas formulas for $j = 0, \ldots, 3$, $s = 0, \ldots, 3$ (see Fig. 8 b)

$$\begin{aligned} \mathbf{p}^5_{2s} &:= \sum_{i=1}^{5} \sum_{j=1}^{2} \mu^s_{ij} \mathbf{d}_{ij} + \sum_{i=1}^{4} \mu^s_{i3} \mathbf{d}_{i3} + \sum_{i=1}^{3} \mu^s_{i4} \mathbf{d}_{i4} \,, \\ \mathbf{p}^6_{1s} &:= \sum_{i=1}^{5} \sum_{j=1}^{2} \mu^s_{6-i,j} \mathbf{d}_{ij} + \sum_{i=1}^{4} \mu^s_{5-i,3} \mathbf{d}_{i3} + \sum_{i=1}^{3} \mu^s_{4-i,4} \mathbf{d}_{i4} \,. \end{aligned} \tag{5}$$

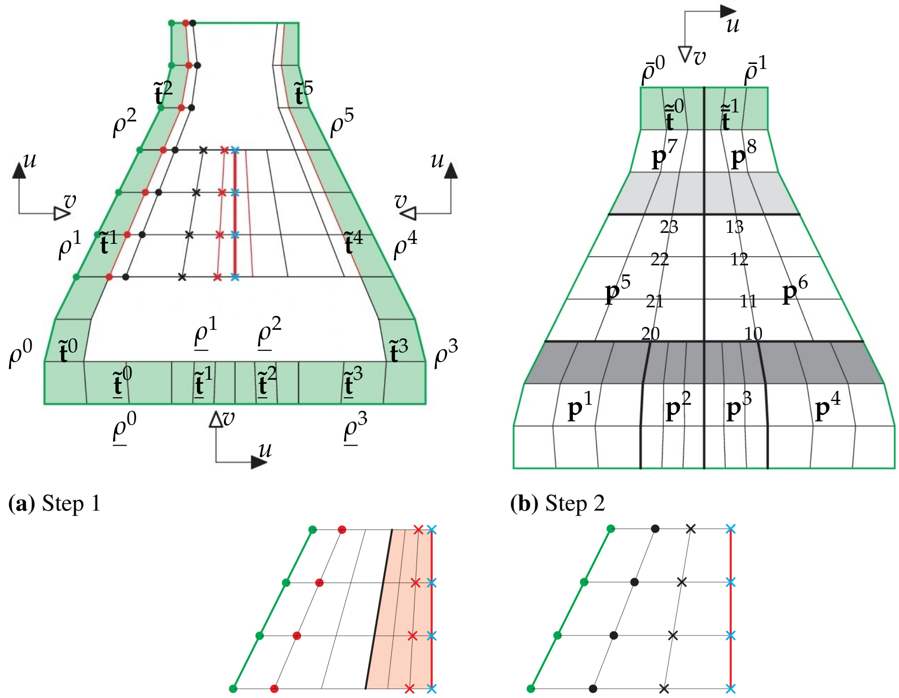

(a) Step 1 **(b)** Step 2

(c) two bi-3 pieces **(d)** merged bi-3 piece

Figure 8. Derivation of the FC^3_8 macro-patch construction and hence of the matrix that defines FC^3_8. Once derived, the implementation of FC^3_8 is just a matrix multiplication.

Without loss of quality, the coefficients μ can be stated with 5 decimals accuracy and corrected by less than 0.00009 to form a partition of 1. That is, the weights μ^s_{ij} listed below are exact, not approximations of the implementation weights.

$$\text{Table } M^s \text{ lists} \quad 10^5 \begin{pmatrix} \mu^s_{14} & \mu^s_{24} & \mu^s_{34} & \times & \times \\ \mu^s_{13} & \mu^s_{23} & \mu^s_{33} & \mu^s_{43} & \times \\ \mu^s_{12} & \mu^s_{22} & \mu^s_{32} & \mu^s_{42} & \mu^s_{52} \\ \mu^s_{11} & \mu^s_{21} & \mu^s_{31} & \mu^s_{41} & \mu^s_{51} \end{pmatrix}.$$

$$M^0 := \begin{pmatrix} 1287 & -2571 & 1287 & \times & \times \\ -896 & 38395 & 15479 & -2979 & \times \\ 4441 & 9437 & 47248 & -13479 & 2358 \\ -428 & 1705 & -2561 & 1705 & -428 \end{pmatrix}, \quad M^1 := \begin{pmatrix} 1952 & -3904 & 1952 & \times & \times \\ 496 & 62003 & 25198 & -4364 & \times \\ 6080 & -9877 & 32592 & -16127 & 3997 \\ -934 & 3739 & -5608 & 3739 & -934 \end{pmatrix},$$

$$M^2 := \begin{pmatrix} 2448 & 12463 & 1753 & \times & \times \\ 6449 & 56051 & 23412 & -2578 & \times \\ 2892 & -12303 & 18821 & -12303 & 2892 \\ -828 & 3315 & -4971 & 3315 & -828 \end{pmatrix}, \quad M^3 := \begin{pmatrix} 8725 & 38797 & 2475 & \times & \times \\ 5059 & 32439 & 13689 & -1190 & \times \\ 1674 & -7179 & 11010 & -7179 & 1674 \\ -531 & 2128 & -3188 & 2128 & -531 \end{pmatrix}.$$

4. Assessments and Comparisons

One motivation of FC^3_8 was to significantly reduce the number of bi-3 patches in FC^3 without overtly harming surface quality. For completeness, we also compare with FP7, a FC construction

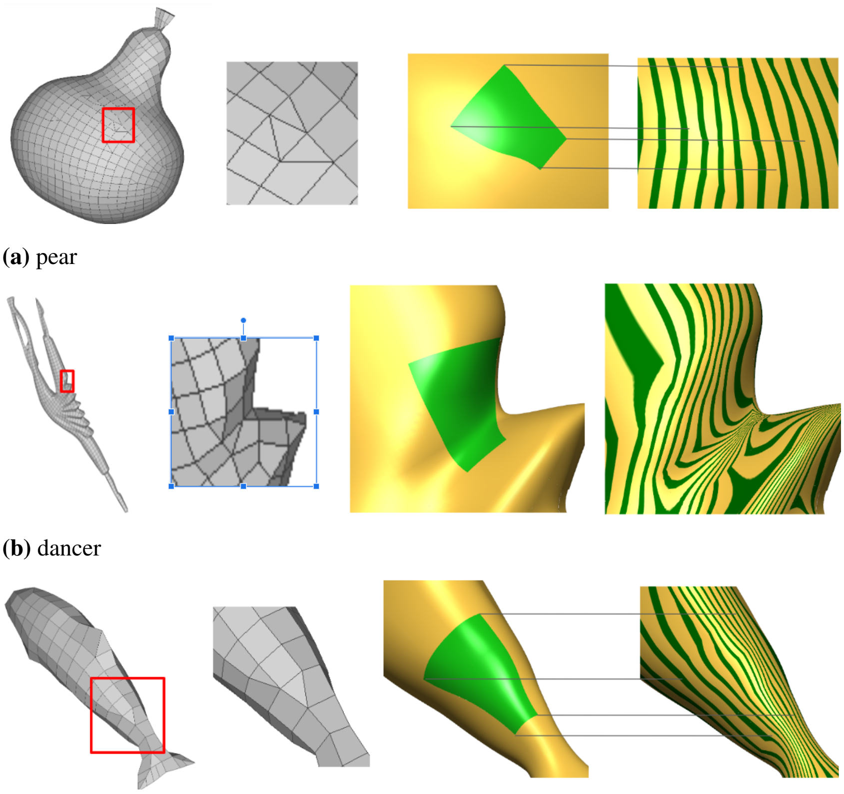

(a) pear

(b) dancer

(c) fish

Figure 9. $\triangle^2$-nets arising in quad-dominant meshing 'in the wild'. Here FC_8^3 is green. Models from www.quadmesh.cloud/Thingi10K [46].

composed of 7 patches, and with FF4, of the same layout as FC^3_8, but pinning down degrees of freedom via the functional $\mathcal{F}_4 := \int_0^1 \int_0^1 \sum_{i+j=4,i,j\geq 0} \frac{4!}{i!j!} (\partial_s^i \partial_t^j f(s,t))^2 \, ds \, dt$.

4.1. Small local challenge nets

Fig. 2 b already introduced the $\triangle^2$-net (nodes marked by $\bullet$) extended by a quad frame whose outermost nodes can be of any valence. While a FC surface is fully defined by $\triangle^2$-net, the extended $\triangle^2$-net yields a regular B-spline bi-2 frame as in Fig. 2 c, and (d,e,f), that reveals any problems in the transition from regular to FC surface. Conversely, the restriction to the extended $\triangle^2$-net avoids the need to zoom-in into area of irregularity on a large model, see e.g. Fig. 9 a and emphasize problematic nets. The nodes of the $\triangle^2$-net shown Fig. 10 a are obtained from the planar layout

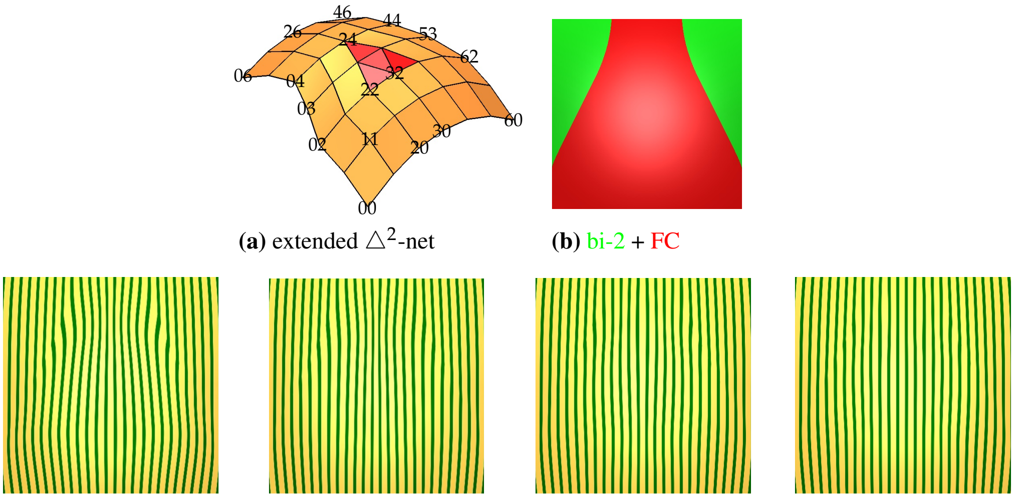

(a) extended $\triangle^2$-net **(b)** bi-2 + FC

(c) FP7 **(d)** FF4 **(e)** FC^3_8 **(f)** FC^3

Figure 10. Comparing FC^3_8 to variants FP7 and FF4, and to its predecessor FC^3. (a) Labels of extended $\triangle^2$-net, see also Fig. 2 a. The highlight line distribution improves from (c)–(f).

of Fig. 2 b by projection onto an elliptic paraboloid. This type of control net is a key when testing surfaces obtained from nets contracting as in Fig. 1 : a high quality surface, similar to an elliptic paraboloid within the region of Fig. 10 b is expected. FP7 displays undesired strong oscillation of the highlight lines, and FF4, as well as FC^3_8 reveals no artifacts under scrutiny, justifying the subtle construction in [6]. Improving on FC^3 is not expected in this specific hard configuration. However, Fig. 11 , Fig. 12 , Fig. 13 show an improvement of FC^3_8 over FC^3 in the highlight line distribution across the transition between patches 5 and 6, respectively and 7 and 8 (see Fig. 6 b for labels), likely due to the increased smoothness when combining the patches into one.

The extended $\triangle^2$-net of Fig. 11 a is derived from Fig. 10 a by lifting a 'horizontal' row of nodes (labels $i3$, $i = 0, \ldots 5$) and a 'vertical' triple ($3j$, $j = 0, 1, 2$) to 32: (b) displays the region shown in (c), (d). Red arrows in Fig. 11 c point to abrupt changes in highlight lines for FC^3 that disappear in FC^3_8, while the $\downarrow$ in Fig. 11 d points to sharper turns in the FC^3_8 highlight lines than in same location for FC^3. The bottom row compares side-views revealing unexpected dips pointed by $\downarrow$ of FF4 and FP7.

The extended $\triangle^2$-net of Fig. 12 is derived from Fig. 10 a by pushing down the nodes with labels ij $i, j = 0, 1, 2$. Red arrows in Fig. 12 c point to abrupt changes in highlight lines for FC^3 that disappear in FC^3_8, while the $\leftarrow$ in Fig. 12 d points to slightly sharper turns in the FC^3_8 highlight lines than in same location for FC^3. The bottom row compares of side-views for FC^3_8 and FP7, revealing an unwanted dip, pointed by $\downarrow$, in FP7. Fig. 13 adds a wavy $\triangle^2$-net commonly occurring in automatically generated meshes. Again, FC^3_8 has a slight shape advantage over FC^3 indicated by $\leftarrow$.

In summary, empirically, we see only a slight (if any) degradation of the highlight line distribution by using fewer pieces in FC^3_8 over FC^3 and an improvement of FC^3_8 over FC^3 in the highlight

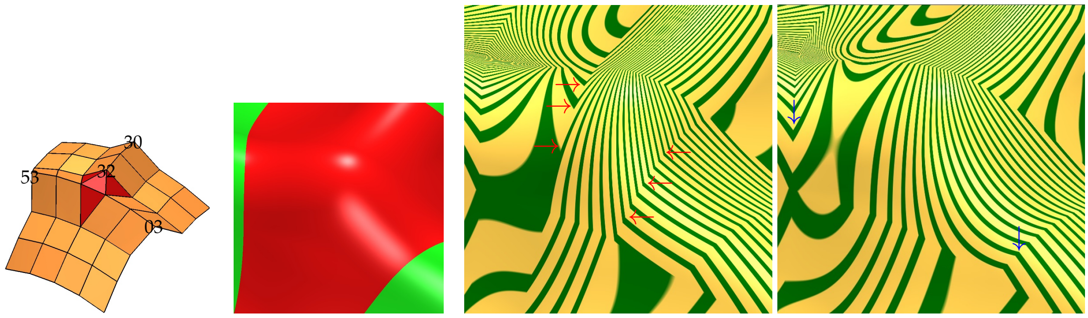

(a) extended $\triangle^2$-net **(b)** bi-2 + FC **(c)** FC^3 **(d)** FC^3_8

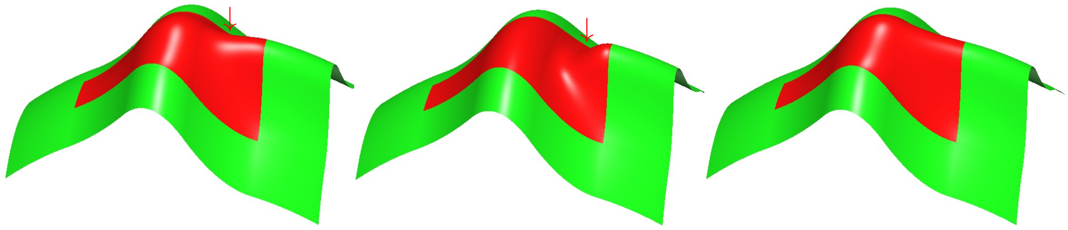

(e) FF4 side-view **(f)** FP7 side-view **(g)** FC^3_8 side-view

Figure 11. Comparing FC^3_8 to variants FP7 and FF4 for ridge preservation.

line distribution across the transition between the merged patches. That is, sharp turns either become considerably milder or disappear.

4.2. Large hand-crafted models

The original motivation of FC^3 (FC^4) was to address local challenges in *re-meshing* for spline surfaces. But the solution lends itself to *direct* design of larger objects, e.g. to design surfaces that start with the ubiquitous shape from revolution such as the examples in Fig. 14 (cf. Fig. 16).

Fig. 15 demonstrates design with $\triangle^2$-nets. The input (a) is a mesh of revolution: the nodes in the 10 horizontal rotational layers lie on co-axially stacked circles. The bottom 4 layers consist of 36 nodes each, the 5th has 24, the 6th and 7th have 12 , the 8th layer 8, and the top two layers have 4 nodes each. The mesh is capped by a quad face, (b) shows the surface layout: the bottom 4 layers become bi-2 patches; the 12 lower and the 4 upper $\triangle^2$-nets become FC^3_8 macro-patches; the four 3-valent vertex neighborhoods at the top are covered by bi-3 patches according to [36]. While the $\triangle^2$-nets overlap, their cores are sufficiently separated to build FC^3_8 macro-patches. Note that (c) contains no sub-mesh defining a bi-2 patch. The second row zooms in on and displays the highlight line distribution of three challenging neighborhoods: (e,f) focuses on the transition between the 12 bottom and 4 top FC^3_8 surfaces; (g,h) on the transition between the 4 top FC^3_8 and the valence 3 neighborhoods; (i,j) on the transition between the regular bi-2 patches and the 12 bottom FC^3_8. The most noticeable changes in the highlight lines occur where regular bi-2 C^1 splines are used, as further discussed later with respect to Fig. 18 c. The bottom row illustrates hand-crafted designs, whose highlight line distributions are on par with regular bi-2 splines.

In Fig. 16 a the rapid merging part of quad strips with $\triangle^2$-nets is taken from Fig. 15 a, while the bottom part (now four quad strips) is modified anticipating a 'connecting tube'. The valence 5 vertices are treated with [36] to yield the smooth transitions in (b). Fig. 16 c,d show a design modification involving the $\triangle^2$-nets.

The goal of Fig. 17 is to compare FC^3_8 for $\triangle^2$-nets to the less rapidly contracting bi-3 surfaces of [8] and to regular C^1 bi-2 splines for designs where any of the three options can be chosen. That is, if FC^3_8 looks no worse than its two alternatives, despite supporting rapid contraction, FC^3_8 passes the test. We recall that [8] takes as input τ_0-nets, namely triangles with two vertices of valence 4 and one with valence 5, surrounded by one layer of quad facets. Row 1 shows surfaces created using [8], and Row 2 regular bi-2 spline surfaces. To make the corresponding surfaces as similar as possible, the 10 layers of (a), (g) Fig. 17 lie on the same circles as for Fig. 15 . The main change is the number of nodes in Fig. 17 : in (a) layers $1, 2, 3, 4$ have 32, layers 5, 6 have 16, layers 7, 8 have 8

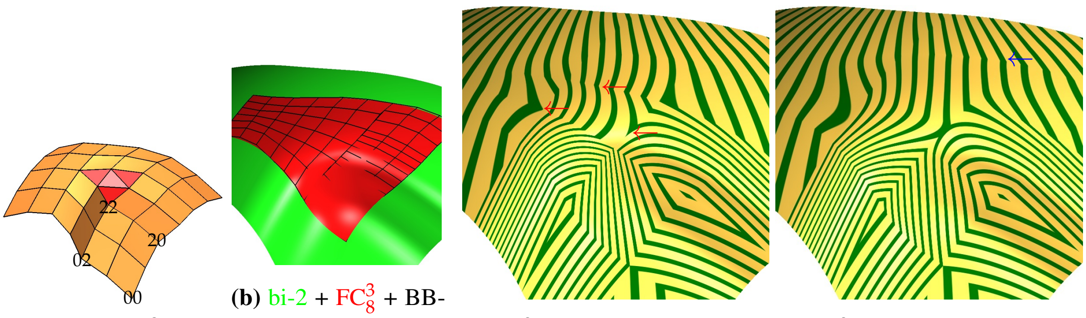

(a) extended $\triangle^2$-net **(b)** bi-2 + FC^3_8 + BB-net **(c)** FC^3 **(d)** FC^3_8

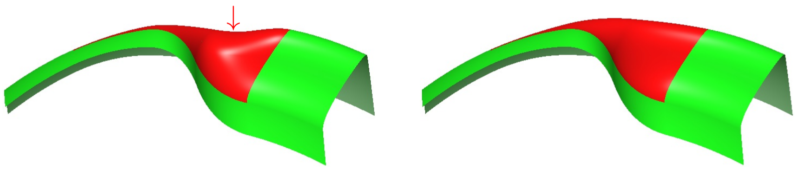

(e) FP7 side-view **(f)** FC^3_8 side-view

Figure 12. Comparing FC^3_8 to FP7 and FC^3 for step-like transition. (b) area of highlight line distribution in (c,d).

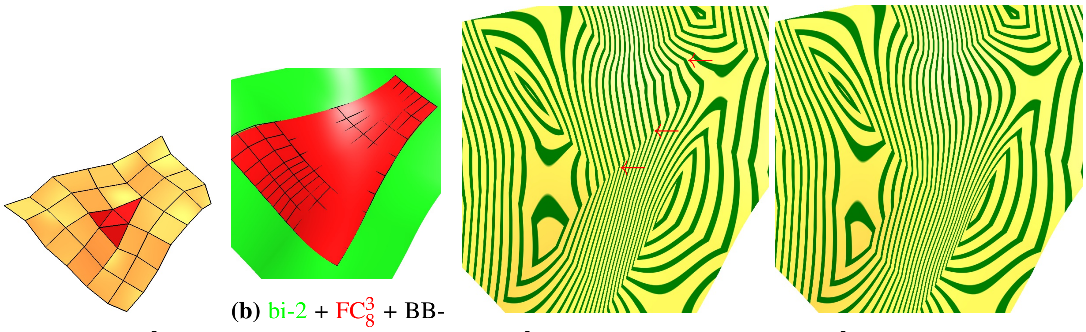

(a) extended $\triangle^2$-net **(b)** bi-2 + FC^3_8 + BB-net **(c)** FC^3 **(d)** FC^3_8

Figure 13. Comparing FC^3_8 to FC^3 on wave-like input.

and layers 9, 10 have 4 nodes; in (g) all layers have 36 nodes. Unlike (a), in the regular mesh (g) the top is not closed: the best option in terms of simplicity and quality) is to cap with 36 triangles sharing a common central vertex, i.e. a polar configuration, see [18] for the details. We omit this cap to focus on the comparison of regular splines with their counterparts based on $\triangle^2$- and τ_0-nets. (Analogously, the cap from Fig. 15 b and Fig. 17 b is omitted displaying the corresponding surfaces in Fig. 17 n,o.) All surfaces in Fig. 15 b, Fig. 17 b,h have the same axial symmetries and similar highlight line distributions, see Fig. 17 m,n,o. That is the highlight line distributions depend on the geometry (large-scale flow) of input meshes more so than on the choice of construction. Modified surfaces can look alike as in Fig. 17 f and Fig. 16 d, or they can differ due to a different layout of τ_0 vs $\triangle^2$ cores (gray in Fig. 1 a,f); see the bottom of Fig. 17 d vs Fig. 15 l. By contrast, the bottom of the regular bi-2 surface Fig. 17 j is very similar to Fig. 15 l; at the top the surface is less of a global shape modification than a local embossing since the corresponding layer in Fig. 15 a has 12, whereas Fig. 17 g has 36 nodes and in each case four nodes are displaced outwards (Fig. 17 k,l displacing by a smaller amount makes a local embossing milder, however an effect of global modification is not achieved). Achieving the effect of FC^3_8 with the un-contracted net is a tricky challenge for a designer as is also if connecting un-contracted tube end to a single quad on the outer disk of Fig. 16 .

Fig. 18 *top* compares the base of Fig. 15 l to the base of Fig. 17 j. The highlight line distributions in Fig. 18 b,c indicate similar surface quality. Also comparing the highlight line distribution of the mid-section, Fig. 18 e,f, shows no clear winner. Indeed, we observe in numerous tests that the quality of FC^3_8 surfaces is no worse than the quality of regular C^1 bi-2 splines, despite the reduction in degrees of freedom.

(a) **(b)** Vilnius *Tube*

Figure 14. Natural occurrence of $\triangle^2$-nets in design. (a) FC_8^3 is green. (b) Modern art installation

5. Conclusion

While very specialized, the optimal treatment of rapid contraction $\triangle^2$-nets by FC_8^3 surfaces is an important building block that allows properly adjusting the parameterization of free-form surfaces when accommodating narrow passages or decrease of detail. Artificially comparing to τ_0-surfaces and regular bi-2 splines where such rapid contraction is not needed shows the FC_8^3 surfaces to be of equal quality and therefore to fit nicely into the Polyhedral-net Spline framework [35].

Author Contributions Conceptualization, Kestutis Karciauskas and Jörg Peters; Data curation, Kestutis Karciauskas and Kyle Lo; Formal analysis, Kestutis Karciauskas and Jörg Peters; Investigation, Kestutis Karciauskas and Erkan Gunpinar; Project administration, Jörg Peters; Software, Kestutis Karciauskas, Kyle Lo and Jörg Peters; Supervision, Jörg Peters; Validation, Kestutis Karciauskas, Kyle Lo, Erkan Gunpinar and Jörg Peters; Visualization, Kyle Lo and Jörg Peters; Writing – original draft, Kestutis Karciauskas and Jörg Peters; Writing – review and editing, Kestutis Karciauskas, Kyle Lo, Erkan Gunpinar and Jörg Peters.

1. Schertler, N.; Tarini, M.; Jakob, W.; Kazhdan, M.; Gumhold, S.; Panozzo, D. Field-Aligned Online Surface Reconstruction. *ACM Trans. Graph.* **2017**, *36*.
2. Jakob, W.; Tarini, M.; Panozzo, D.; Sorkine-Hornung, O. Instant Field-Aligned Meshes. *ACM Trans. Graph.* **2015**, *34*.
3. Doo, D.; Sabin, M. Behaviour of recursive division surfaces near extraordinary points. *Computer-Aided Design* **1978**, *10*, 356–360.
4. Karčiauskas, K.; Peters, J. Point-augmented biquadratic C^1 subdivision surfaces. *Graphical Models* **2015**, *77*, 18–26.
5. Karčiauskas, K.; Peters, J. Localized remeshing for polyhedral splines. *Computers & Graphics* **2022**, *106*, 58–65.
6. Gunpinar, E.; Karčiauskas, K.; Peters, J. Splines for fast-contracting polyhedral control nets. In Proceedings of the Solid and Physical Modelling, 2024, pp. 1–12.
7. Karčiauskas, K.; Peters, J. Refinable smooth surfaces for locally quad-dominant meshes with T-gons. *Computers & Graphics* **2019**, *82*, 193–202.
8. Karčiauskas, K.; Peters, J. Low degree splines for locally quad-dominant meshes. *Computer Aided Geometric Design* **2020**, *83*, 101934.
9. Catmull, E.; Clark, J. Recursively generated B-spline surfaces on arbitrary topological meshes. *Computer-Aided Design* **1978**, *10*, 350–355.
10. Salvi, P.; Várady, T. Multi-sided surfaces with fullness control. In Proceedings of the Proceedings of the Eighth Hungarian Conference on Computer Graphics and Geometry, 2016, pp. 61–69.
11. Hettinga, G.J.; Kosinka, J. A multisided C^2 B-spline patch over extraordinary vertices in quadrilateral meshes. *Computer-Aided Design* **2020**, *127*, 102855.
12. Vaitkus, M.; Várady, T.; Salvi, P.; Sipos, Á. Multi-sided B-spline surfaces over curved, multi-connected domains. *Computer Aided Geometric Design* **2021**, *89*, 102019.
13. Karčiauskas, K.; Peters, J. Point-augmented bi-cubic subdivision surfaces. In Proceedings of the Pacific Graphics 2022; Umetani, N.; Vouga, E.; Wojtan, C., Eds. The Eurographics Association and John Wiley & Sons Ltd., pp. 1–11.
14. Karčiauskas, K.; Peters, J. Evolving Guide Subdivision. *Computer Graphics Forum* **2023**, *42*, 321–332.

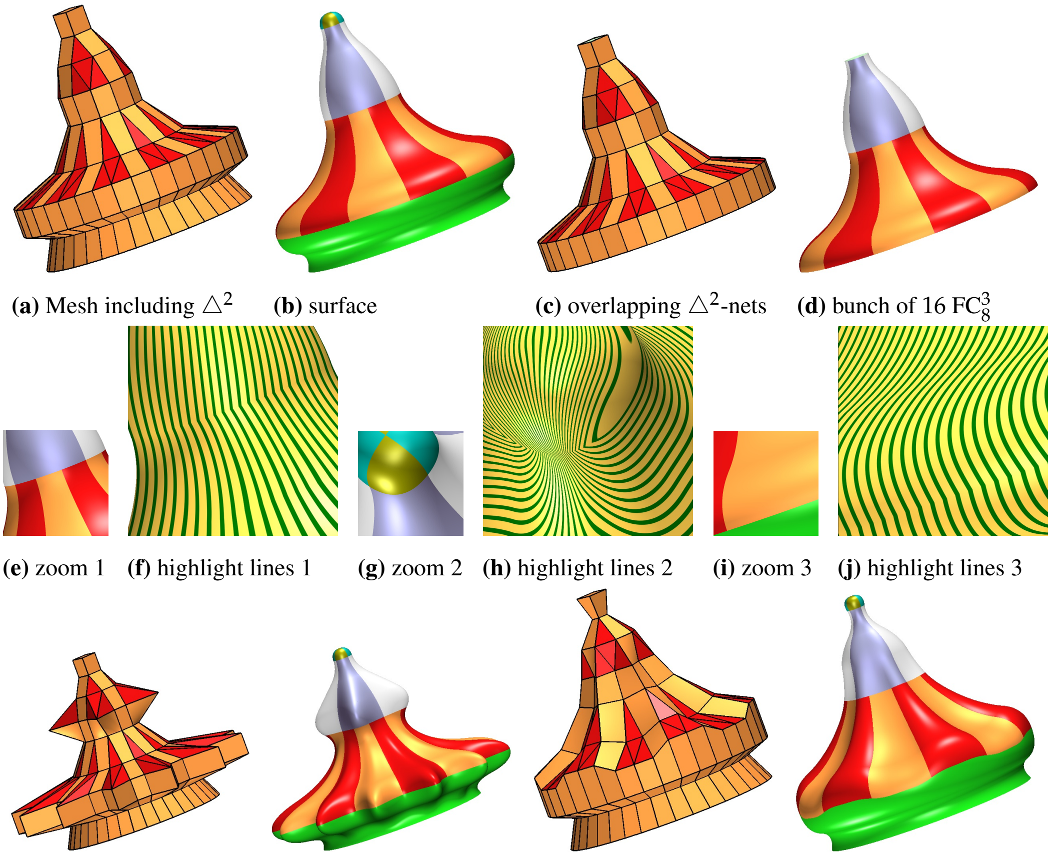

(a) Mesh including $\triangle^2$ **(b)** surface **(c)** overlapping $\triangle^2$-nets **(d)** bunch of 16 FC_8^3

(e) zoom 1 **(f)** highlight lines 1 **(g)** zoom 2 **(h)** highlight lines 2 **(i)** zoom 3 **(j)** highlight lines 3

(k) modified mesh 1 **(l)** modified surface 1 **(m)** modified mesh 2 **(n)** modified surface 2

Figure 15. Overlapping $\triangle^2$ nets. (c) shows the sub-net of (a) that consists entirely of overlapping $\triangle^2$-nets. That is, the surface in (d) consists entirely of FC_8^3 macro-patches.

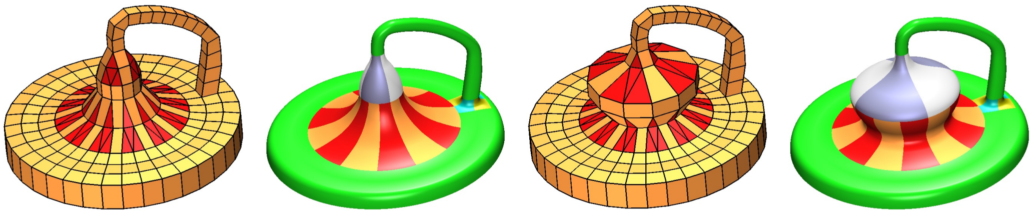

(a) mesh with tube **(b)** surface with tube **(c)** modified mesh **(d)** modification surface

Figure 16. Design inspired by Fig. 14 b.

15. Karčiauskas, K.; Peters, J. Quadratic-Attraction Subdivision. *Computer Graphics Forum* **2023**, *42*, e14 900.
16. Myles, A.; Peters, J. C^2 Splines Covering Polar Configurations. *Computer Aided Design* **2011**, *43*, 1322–1329.
17. Toshniwal, D.; Speleers, H.; Hiemstra, R.R.; Hughes, T.J. Multi-degree smooth polar splines: A framework for geometric modeling and isogeometric analysis. *Computer Methods in Applied Mechanics and Engineering* **2017**, *316*, 1005–1061.
18. Karčiauskas, K.; Peters, J. Smooth polar caps for locally quad-dominant meshes. *Computer Aided Geometric Design* **2020**, *81*, 1–12.
19. Peters, J. Parametrizing singularly to enclose vertices by a smooth parametric surface. In Proceedings of the Graphics Interface '91, Calgary, Alberta, 3–7 June 1991:; MacKay, S.; Kidd, E.M., Eds., 243 College St, 5th Floor, Toronto, Ontario M5T 2Y1, Canada, 1991; pp. 1–7.
20. Reif, U. A refineable space of smooth spline surfaces of arbitrary topological genus. *Journal of Approximation Theory* **1997**, *90*, 174–199.
21. Nguyen, T.; Karčiauskas, K.; Peters, J. C^1 finite elements on non-tensor-product 2d and 3d manifolds. *Applied Mathematics and Computation* **2016**, *272*, 148–158.

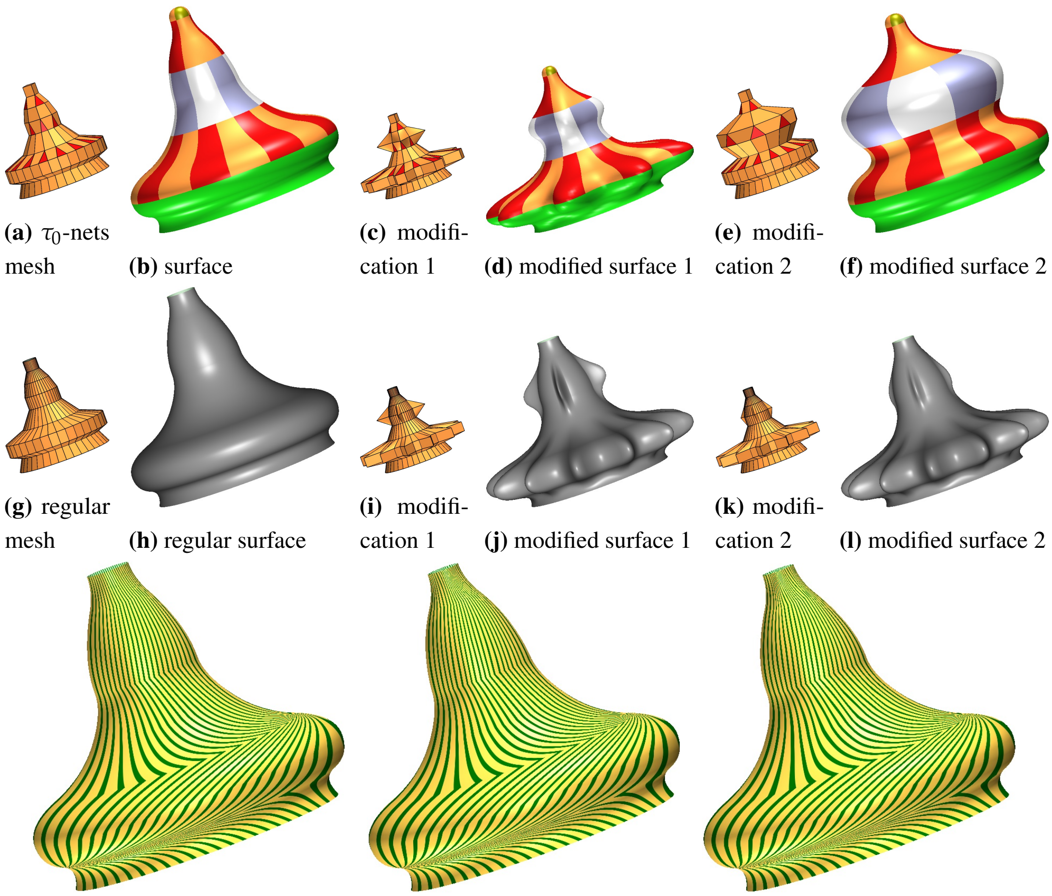

(a) τ_0-nets mesh **(b)** surface **(c)** modification 1 **(d)** modified surface 1 **(e)** modification 2 **(f)** modified surface 2

(g) regular mesh **(h)** regular surface **(i)** modification 1 **(j)** modified surface 1 **(k)** modification 2 **(l)** modified surface 2

(m) regular net surface (h) **(n)** contracting net surface (b) **(o)** $\triangle^2$-net FC^3_8 surface Fig. 15 b

Figure 17. Designs mimicking Fig. 15 but using τ_0-nets or regular bi-2 splines. (m,n,o) visual equivalence of un-contracted, moderate-speed-contracted and fast-contracted surfaces.

22. Wei, X.; Zhang, Y.J.; Toshniwal, D.; Speleers, H.; Li, X.; Manni, C.; Evans, J.A.; Hughes, T.J. Blended B-spline construction on unstructured quadrilateral and hexahedral meshes with optimal convergence rates in isogeometric analysis. *Computer Methods in Applied Mechanics and Engineering* **2018**, *341*, 609–639.
23. Gregory, J.A., Smooth interpolation without twist constraints. In *Computer Aided Geometric Design*; Barnhill, R.E.; Riesenfeld, R.F., Eds.; Academic Press, 1974; pp. 71–88.
24. Loop, C.T.; Schaefer, S.; Ni, T.; Castaño, I. Approximating subdivision surfaces with Gregory patches for hardware tessellation. *ACM Trans. Graph* **2009**, *28*, 151:1–151:9.
25. Loop, C.T.; Schaefer, S. G^2 Tensor Product Splines over Extraordinary Vertices. *Comput. Graph. Forum* **2008**, *27*, 1373–1382.
26. Karčiauskas, K.; Peters, J. Minimal bi-6 G^2 completion of bicubic spline surfaces. *Computer Aided Geometric Design* **2016**, *41*, 10–22.
27. Karčiauskas, K.; Peters, J. Improved shape for multi-surface blends. *Graphical Models* **2015**, *82*, 87–98.
28. Kapl, M.; Sangalli, G.; Takacs, T. Dimension and basis construction for analysis-suitable G^1 two-patch parameterizations. *Computer Aided Geometric Design* **2017**, *52-53*, 75–89.
29. Blidia, A.; Mourrain, B.; Xu, G. Geometrically smooth spline bases for data fitting and simulation. *Computer Aided Geometric Design* **2020**, *78*, 101814.
30. Marsala, M.; Mantzaflaris, A.; Mourrain, B. G1-Smooth biquintic approximation of Catmull-Clark subdivision surfaces. *Computer Aided Geometric Design* **2022**, *99*, 102158.
31. Karčiauskas, K.; Peters, J. Bi-cubic scaffold surfaces. Solid and Physical Modeling (SpM 22), 2022, pp. 1–10.
32. Bonneau, G.P.; Hahmann, S. Flexible G^1 interpolation of quad meshes. *Graphical Models* **2014**, *76*, 669–681.
33. Karčiauskas, K.; Nguyen, T.; Peters, J. Generalizing bicubic splines for modeling and IGA with irregular layout. *Computer-Aided Design* **2016**, *70*, 23–35.

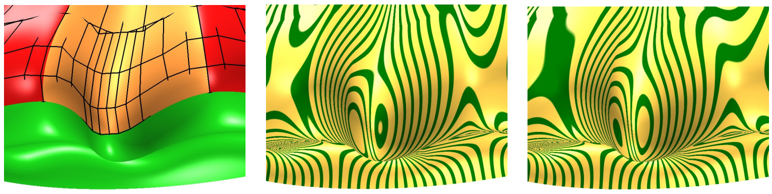

(a) Fig. 15 l bottom **(b)** Fig. 15 l bottom **(c)** Fig. 17 j bottom

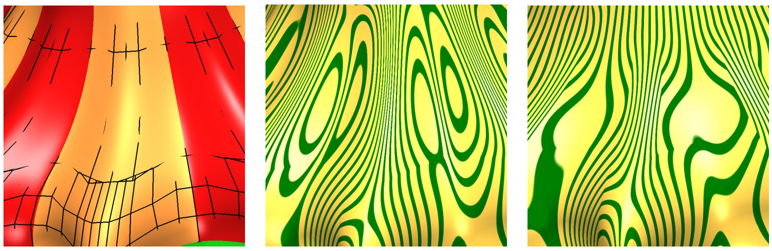

(d) Fig. 15 l middle **(e)** Fig. 15 l middle **(f)** Fig. 17 j middle

Figure 18. Detailed comparison of surfaces Fig. 15 (l) and Fig. 17 (j).

34. Beier, K.P.; Chen, Y. Highlight-line algorithm for realtime surface-quality assessment. *Computer-Aided Design* **1994**, *26*, 268–277. Special Issue: Mathematical methods for CAD.
35. Peters, J.; Lo, K.; Karčiauskas, K. Algorithm 1032: Bi-cubic splines for polyhedral control nets. *ACM Tr on Math Software* **2023**, *49*.
36. Karčiauskas, K.; Peters, J. Smooth multi-sided blending of biquadratic splines. *Computers & Graphics* **2015**, *46*, 172–185.
37. Karčiauskas, K.; Peters, J. Low degree splines for locally quad-dominant meshes. *Computer Aided Geometric Design* **2020**, *83*, 1–12.
38. Sederberg, T.W.; Zheng, J.; Bakenov, A.; Nasri, A. T-splines and T-NURCCs. In Proceedings of the Proc ACM SIGGRAPH; Hodgins, J.; Hart, J.C., Eds., 2003, Vol. 22(3), *ACM Tr Graph*, pp. 477–484.
39. Karčiauskas, K.; Panozzo, D.; Peters, J. T-junctions in spline surfaces. *ACM Tr on Graphics* **2017**, *36*, 170:1–9.
40. Campen, M.; Zorin, D. Similarity maps and field-guided T-splines: a perfect couple. *ACM Trans. Graph* **2017**, *36*, 91:1–91:16.
41. Tong, Y.; Alliez, P.; Cohen-Steiner, D.; Desbrun, M. Designing quadrangulations with discrete harmonic forms. In Proceedings of the Eurographics symposium on geometry processing, 2006.
42. Peng, C.H.; Barton, M.; Jiang, C.; Wonka, P. Exploring quadrangulations. *ACM Transactions on Graphics (TOG)* **2014**, *33*, 1–13.
43. Bommes, D.; Campen, M.; Ebke, H.C.; Alliez, P.; Kobbelt, L. Integer-grid maps for reliable quad meshing. *ACM Transactions on Graphics (TOG)* **2013**, *32*, 1–12.
44. Farin, G. *Curves and Surfaces for Computer Aided Geometric Design: A Practical Guide*; Academic Press, 1988.
45. DeRose, T.D. Necessary and sufficient conditions for tangent plane continuity of Bézier surfaces. *Comp Aid Geom Design* **1990**, *7*, 165–179.
46. Pietroni, N.; Nuvoli, S.; Alderighi, T.; Cignoni, P.; Tarini, M.; et al. Reliable feature-line driven quad-remeshing. *ACM Transactions on Graphics* **2021**, *40*, 1–17.